TURBOMACHINERY & PUMP SYMPOSIA | HOUSTON, TX
DECEMBER 14-16, 2021
SHORT COURSES: DECEMBER 13, 2021

STABILITY ANALYSIS OF A MULTI-STAGE GAS COMPRESSOR WITH SWIRL-BRAKES USING THREE DIMENSIONAL TRANSIENT CFD MODEL

Eunseok Kim
Solar Turbines Inc.,
San Diego, CA, USA

Balaji Venkataraman
Solar Turbines Inc.,
San Diego, CA, USA

Eunseok Kim is a Principal Design Engineer in the Rotordynamics Group at Solar Turbines, Inc. He holds a PhD in Mechanical Engineering from Texas A&M University and joined Solar in 2017. His previous work focused on rotordynamic stability evaluation of centrifugal pump impellers using CFD. His current work includes rotordynamic analysis and testing of gas compressors, swirl brakes and damper seal designs using CFD techniques.

Balaji Venkataraman is the Manager of Rotordynamics, Gas Compressor Products at Solar Turbines, Inc. He has been with Solar for over 22 years. His group is responsible for rotordynamic design, testing, field reliability and product quality of compressors from vibration standpoint. Balaji has extensive experience in vibrations, troubleshooting and resolution of vibration issues, seal design and damper bearings. Prior to joining Solar, Balaji worked for Atlas Copco and was a visiting researcher at NASA's Marshall Space Flight Center, Huntsville, AL. Balaji holds a master's degree in Mechanical Engineering from Texas A&M University.

ABSTRACT

Minimizing fluid induced forces through the secondary leakage flow paths in shrouded centrifugal impellers is crucial to improve the rotordynamic stability of high-pressure centrifugal gas compressors. Swirl brakes (SBs) are widely used in turbomachinery to reduce the fluid induced forces and enhance the system rotordynamic behavior. Prior to the present study, swirl-brakes of a high-pressure multi-stage compressor were designed using 3D steady-state computational fluid dynamics (CFD) analysis and verified through multiple full-scale closed loop tests for a compressor, operating with and without the SBs.

In the present study, a 3D transient CFD analysis is conducted to calculate the fluid induced rotordynamic coefficients of a Teeth-on-Rotor (TOR) seal and the impeller shroud cavity. Full 360° fluid domains including the impeller, the shroud cavity, and TOR seals with either a swirl-brake or without it are numerically modeled. A mesh deformation technique is employed to follow the whirling rotor motion of the impeller. To evaluate the capability of the transient CFD model, comparisons are made between the prior test results and predictions from the current numerical study.

The cross-coupled destabilizing forces as calculated from CFD are then compared with the methodologies recommended by API 617 and a few other researchers in the literature. In addition, the destabilizing forces calculated through the CFD methodology are used in rotordynamic simulations of the rotor, with and without SBs. Comparisons of simulation results to test results and field performance show good qualitative correlation. CFD predicts forces in the secondary flow path (without SBs) that cause early signs of instability observed in the compressor. The same methodology with SBs predicts cross-coupling forces that are benign, which is also confirmed by stable operation of the same compressor when rebuilt with SBs. These results are included in the paper.

INTRODUCTION

Predicting fluid induced forces is a critical step in evaluating the rotordynamic stability of turbomachinery. Much research has been carried out to build more accurate models for the simulation of fluid induced forces. Wachel and von Nimitz [1] developed an empirical equation (Wachel formula) to calculate an aerodynamic cross coupling force from gas compressor stages. In API 617 [2], a modified

Wachel formula evaluates the stability of centrifugal compressors to meet the Level I screening Criteria. Childs [3] has employed a bulk flow model of the leakage path of a pump impeller and compared the predicted rotordynamic coefficients against test results published by Bolleter et al. [4]. While the bulk flow model predicted the direct damping well when compared to the test results, the other predicted coefficients varied by larger than 50% from the measured data. Moore and Palazzolo [5] utilized an eccentric steady state CFD model to predict destabilizing forces in a shrouded pump impeller. Moore et al. [6] applied the eccentric steady state CFD model to a gas compressor to develop analytical expressions for direct and cross coupled stiffnesses of centrifugal compressors and suggested a new form of the cross-coupled stiffness formulated from CFD parametric runs. The steady state CFD model [5] showed improved predictions compared to the bulk flow model of Childs [3], however, the quasi-steady state solution did not simulate time dependent relative motion between stationary and rotating fluid domains.

Chochua et al. [7] predicted the rotordynamic coefficients of a hole pattern seal using a transient CFD analysis with one-direction translational movement. Xin et al. [8] utilized periodic circular orbit model for the transient analysis and compared the results with the bulk flow analysis and the one-direction translational model. Li et al. [9] expanded the circular orbit model to multiple frequency elliptical whirling orbit model and calculated the frequency dependent rotordynamic coefficients using the Fast Fourier Transform. Yan et al. [10] employed Laplace transform and mathematical deductions to calculate the frequency dependent rotordynamic coefficients from one or two transient force predictions. More recently, Hoopes et al. [11] predicted the frequency dependent and frequency independent coefficients for an axisymmetric impeller shroud cavity utilizing a transient moving wall CFD method and showed the capability of the transient CFD approach to predict the rotordynamic coefficients.

Swirl in the secondary flow path of a centrifugal impeller is one of main sources of rotordynamic instability problem in turbomachinery. The swirl ratio at the inlet of the labyrinth eye seals have been shown in the literature to have a strong influence on the destabilizing forces. Hence, it is important to reduce the swirl in the secondary flow path of the impeller and at the entry of the eye seals to improve the stability of centrifugal compressors using shrouded impellers. To achieve stability improvement of turbomachinery, SBs have been employed to suppress the circumferential velocity inside the flow path along the annular seals and secondary leakage flow paths. Several studies on SBs have been performed and the capabilities of SBs were effectively explained using CFD analysis. Nielsen et al. [12] optimized SBs of a centrifugal pump by estimating swirl ratios along the secondary leakage flow path using a 3D Navier-Stokes solver. Moore and Hill [13] modeled a 3D centrifugal impeller CFD model to capture swirl reduction effect by SBs located inside of the secondary leakage flow path and optimized the SBs to make negative swirl at the eye seal inlet. Baldassarre et al. [14] utilized CFD approach to optimize SB dimensions by evaluating swirl ratios at the labyrinth seal inlet and calculated pre-swirl at the seal inlet through comparison of the log-decs between predictions and measurements.

Using steady state CFD analysis, Venkataraman et al. [15] designed and optimized SBs for a multi-stage compressor. These SBs were evaluated through a series of tests that showed reduced swirl ratio and improved stability. However, the steady state predictions could not calculate the rotordynamic coefficients due to the non-axisymmetric SB geometry. The current effort extends the work done in [15] by analyzing an asymmetric geometry of an impeller shroud cavity with SBs and predicts the rotordynamic coefficients of the shroud cavity including the impeller eye seal for a TOR configuration. In this paper, a full 360^o transient CFD analysis was employed. A transient mesh deformation technique was utilized in the analysis due to the asymmetric feature of the SBs. The transient moving mesh model could effectively simulate the actual physical motion of the whirling rotor. Performance of the SBs was investigated through comparisons of the rotordynamic coefficients between the results without SBs (Baseline model) and with SBs (SB model). The predicted cross-coupled stiffness was compared with empirical equations in [1] and [2] and the developed cross coupling formula from the parametric CFD study [6].

Finally, the cross-coupling forces calculated by the empirical equations and the CFD analysis were utilized to perform the rotordynamic stability analysis per API 617. Predicted log decs were compared and reviewed to evaluate the capability of the transient CFD analysis for modeling turbomachinery with asymmetric feature and evaluating the rotordynamic stability.

BACKGROUND

The motivation for the work presented in this paper arises from the uncertainty levels experienced in quantifying destabilizing forces in high-pressure centrifugal compressors and even more so, when proven techniques (like SBs or hole-pattern seals) are employed to mitigate instability risks. Multiple methods have been proposed in the literature to estimate cross-coupling forces (Wachel [1], API 617 [2], Moore et al. [6]), but they tend to be empirical and are subject to large uncertainties in determining if a rotor would be stable or not. This stability assessment becomes critical especially when end-users rightfully want to operate the compressors far beyond their original intent, e.g., higher speeds and operating pressures based on process demands. Original equipment manufacturers (OEMs) must assess risk accurately or provide strong risk mitigating solutions considering the uncertainty. Such a situation presented itself to the OEM when an end-user wanted to move the operating point of a compressor (that was running fine for over 17 years) to a significantly challenging operating point. High-pressure turbomachinery traditionally uses SBs to improve rotordynamic stability; hence the OEM and the end-user agreed to design and install SBs for this application.

Experimental measurements of swirl obtained in sub-scale testing of a scaled stage showed a significant reduction of swirl with swirl-brakes (TOR configuration). The measured swirl velocity matched analytical predictions produced by a steady-state CFD analysis [15]. Both these results were confirmed by a full-scale closed loop test for a six-stage rotor. The test was performed with and without SBs multiple times to ensure repeatability. Rotor radial and axial vibrations were monitored during the tests with proximity probes installed near the journal bearings. Figure 1(a) shows the measured unstable vibrations without SBs. However, the compressor impeller seals with SBs showed stable behavior without instability when it ran at identical conditions, as shown in Figure 1(b). The full-scale testing satisfied the end-user requirements.

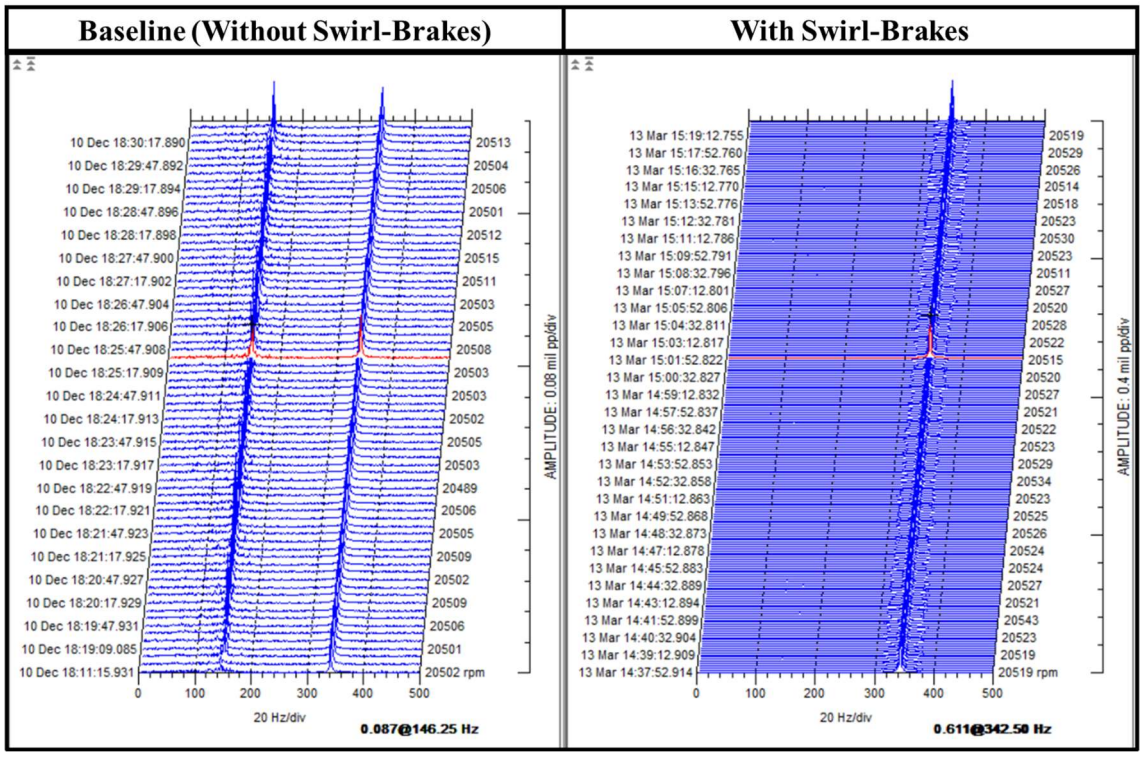

(a) Compressor seals w/o SBs (b) Compressor seals with SBs

Figure 1. Full-scale testing results at rated condition, 20522rpm [15] (a) w/o SBs, and (b) with SBs

With practical applications of SBs proving to be quite successful, the need for accurately predicting the force coefficients of SBs during the design phase of a rotor becomes essential. Simulation of SBs (both for design and performance improvement purposes) has depended heavily on CFD. The analysis must incorporate the rotor-stator interaction between the rotating component (seal teeth on a TOR configuration) and the stator (swirl-brakes and the abradable sealing surface). A full 360°, non-axisymmetric, concentric-rotor model was employed; and a moving mesh of the rotor-stator surface was created for the analysis. The impellers analyzed in this paper are 2nd and 5th stages used in the tested compressor. Figure 2 shows the rotor is supported by two tilt-pad journal bearings, a balance piston seal and employs dry gas seals for process gas containment.

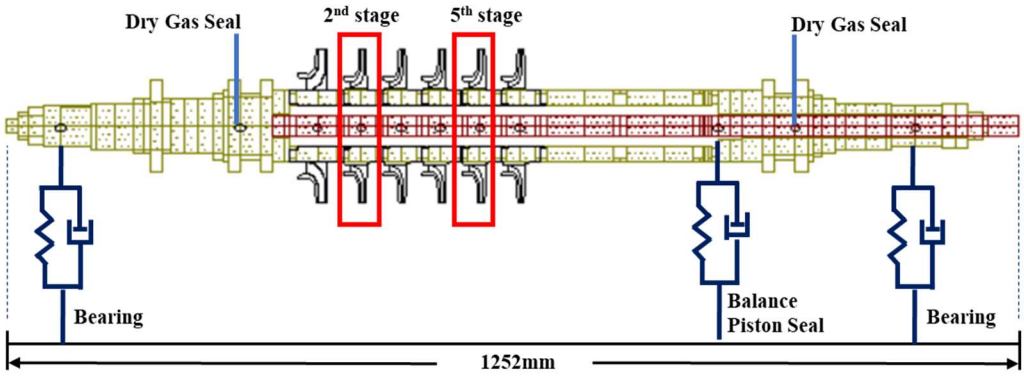

Figure 2. Rotor model of the 6-stage compressor

3D MODEL/MESH GENERATION

Venkataraman et al. [15] detail the design of the SB and TOR neck-ring (eye ring) seal. The number of slots (vanes) was 61, based on the optimization using steady state CFD analysis with a pie-slice model. The SB location is up-stream of the impeller eye seal to reduce, even suppress, the inlet swirl entering the seal. To avoid rubbing between the seal edge and the front shroud surface of the impeller, the location of the SB was placed at the region above the first labyrinth tooth. A full 360° concentric impeller model was constructed to perform the transient CFD analysis. Figure 3 shows the cross section of the full 360 ° front shroud cavity model with the optimized SBs. The detailed dimensions of the SBs can be found in Ref. [15]. Table 1 indicates eye seal geometry. A Baseline 3D model was also created without the SBs for the comparison case.

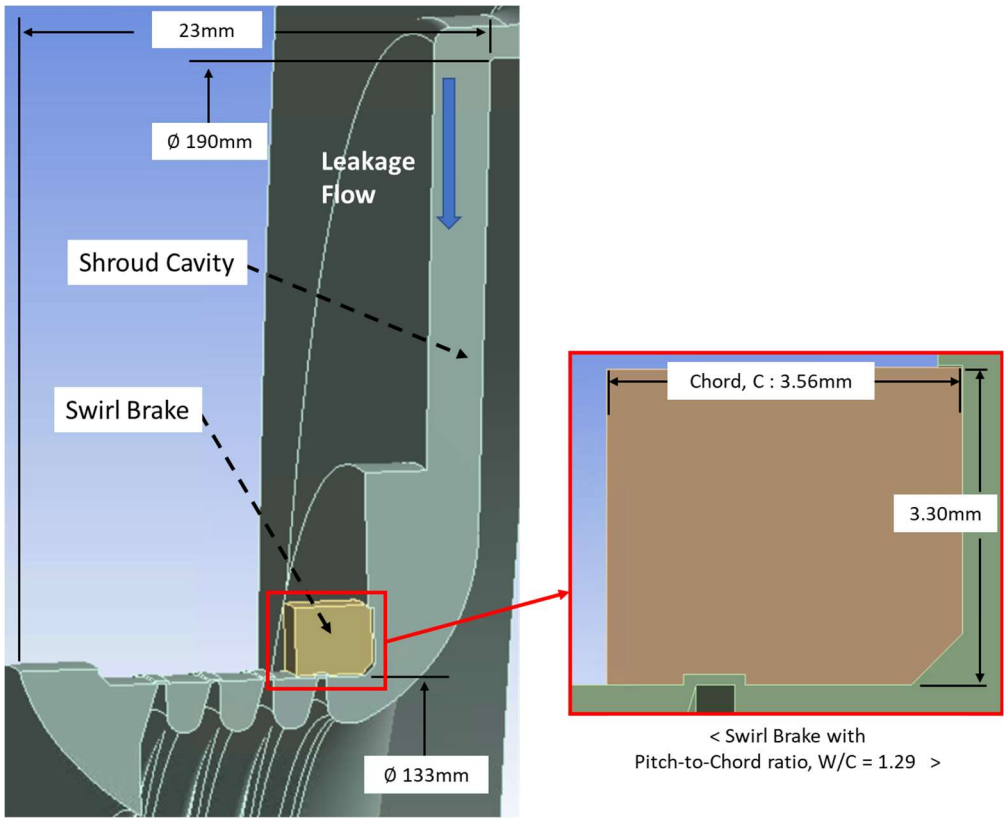

Figure 3. Shroud Cavity Leakage Flow Path with Swirl-Brakes, Optimized Design

Table 1. Eye seal geometry

	Unit [mm]
Seal Radius	66.7
Tooth Pitch	2.9
Tooth Height	2.3
Seal Clearance	0.11
Number of Teeth	4

Figure 4 and Figure 5 show the mesh for the fluid domains of the selected stage in the compressor. The utilized grid model was composed of five domains: Inlet, Impeller, Diffuser, Front Shroud Cavity, and Swirl-Brakes. The impeller back surface shroud cavity was ignored in the transient CFD model because the influence on the destabilizing forces at this location is negligible compared to the forces from the front cavity [4]. Each domain was modeled and meshed separately; then, they were combined in the pre-processor module with five domain interfaces. A face mesh with quadrilateral or triangular elements was generated on each domain and swept around the spinning rotor axis. With a swept mesh, the full 360 ° grid models could be generated for each of the five domains.

In the transient CFD analysis, the shroud surface in the shroud cavity domain was defined as a moving wall, hence allowing mesh

deformation. The moving shroud surface includes the eye seal. Due to the tight clearance of the eye seal, negative volume elements could occur during the transient rotor whirling motion. Thus, care was taken to prevent such error. The inflation layers in the eye seal were generated to allocate 20 layers in the seal radial clearance. The mesh near the wall was sized to achieve $y+$ values < 50, where $y+$ is a dimensionless wall distance.

The mesh was generated with prism and hexahedral elements. Table 2 details the mesh size for each domain. Over 80% mesh nodes were assigned to the shroud cavity domain and the SB domain. The mesh size was determined based on a previous optimization work for the front cavity with the SBs [15]. The required computational time for a case was about 5 hours using 280 cores with Intel Xeon® 64 processors.

Table 2. Summary of 3D Mesh

Domain	Number of Nodes
Inlet	502,200
Impeller	1,963,728
Diffuser	725,460
Shroud Cavity	14,373,678
SBs	2,812,320

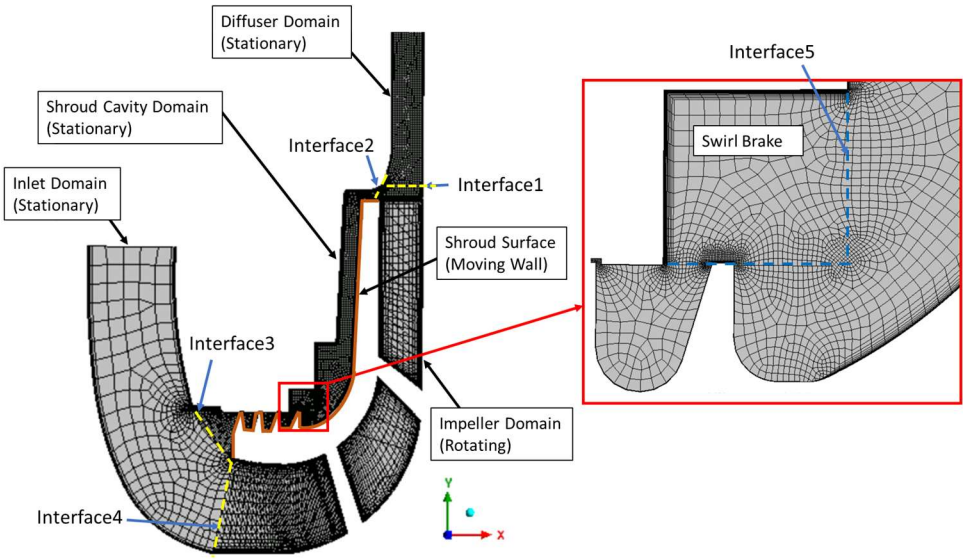

Figure 4. Cross-Section of 3D mesh

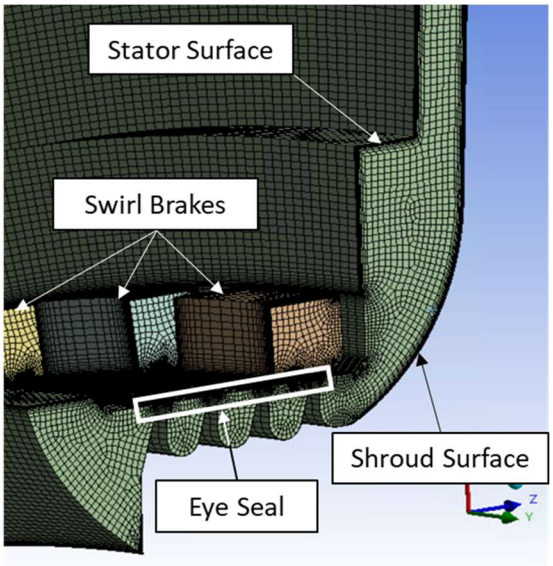

Figure 5. 3D front cavity mesh showing vanes in SB and teeth on rotor.

BOUNDARY CONDITIONS

The boundary conditions for the CFD analysis were chosen from the measured data [15] when the compressor operating without the SBs showed unstable behavior. Table 3 shows the boundary conditions for the 2nd stage.

Table 3. Boundary conditions (2nd stage)

Shaft Rotational Speed	20,522 [rpm]
Inlet Pressure	6.70 [MPa]
Inlet temperature	36 [℃]
Density at Inlet	66 [kg/m^3]
Outlet Pressure	8.20 [MPa]
Outlet Mass Flow Rate	9.48 [kg/s]
Fluid Density at Outlet	74 [kg/m^3]

The pre-swirl at the inlet domain to the impeller stage was ignored due to the presence of flow-straightening vanes up-stream of each impeller inducer. The total pressure was imposed at the inlet along with a turbulence intensity of 5%, and the mass flow rate with a uniform mass flux was defined at the outlet of the diffuser domain, as shown in Table 3. All the walls were assumed to be no-slip and adiabatic. The analysis used the k-ω based Shear Stress Transport (SST) model. The SST turbulence model was chosen because it provides improved near wall treatment compared to the standard $k-\varepsilon$ model [16].

NUMERICAL MODEL FOR TIME TRANSIENT CFD ANALYSIS

The impeller domain in Figure 4 was defined as a rotating domain, whereas the other domains were defined as stationary domains. Since the rotating impeller domain has a relative motion with respect to the stationary domains, transient sliding interfaces were defined at Interface2 and Interface4 of Figure 4. The other interfaces between the stationary frames were defined as generalized grid interfaces.

The shroud cavity domain motion is described in Figure 6. The shroud surface is rotating about its geometric center, while the impeller is whirling about the whirling center. To achieve the domain motion of Figure 6, the shroud surface in the shroud cavity domain was defined as a rotating wall in this study. The whirling motion of the shroud surface was achieved by specifying the mesh deformation with the rotor displacements. The rotor displacements in *X* and *Y* directions are represented by a circular whirling orbit with periodicity and defined by

$$X = A\cos(\Omega t)$$
$$Y = A\sin(\Omega t) \quad (1)$$

where *A* is the radius of the circular orbit, and $\Omega=2\pi f$ is the excitation whirl frequency. When the shroud surface moves with the defined periodic displacements, the grids of the shroud cavity are deformed from the initial grid.

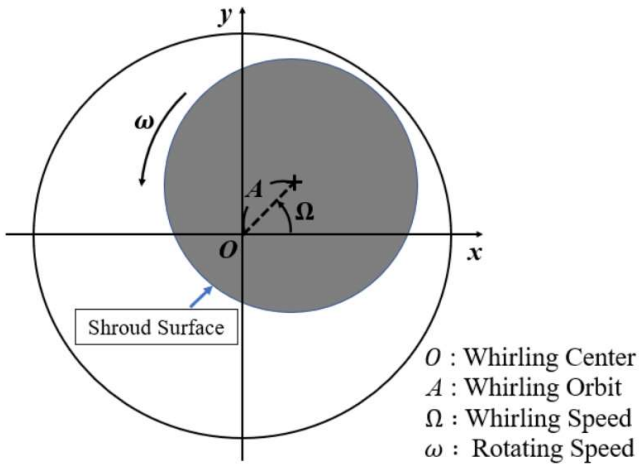

Figure 6. Whirling Rotor of Shroud Cavity Domain

SWIRL RATIO CALCULATION

To validate the generated grid model with SBs, a time transient CFD analysis was performed with the rotor at a centered position and applying no whirling motion. A centered, concentric mesh was used since the rotor could be off centered by deforming the shroud cavity mesh during the transient CFD analysis. The imposed offset was 50% of the seal clearance. The full 360° transient analysis provided the fluid swirl velocities for both Baseline (without Swirl Brakes) and SB models.

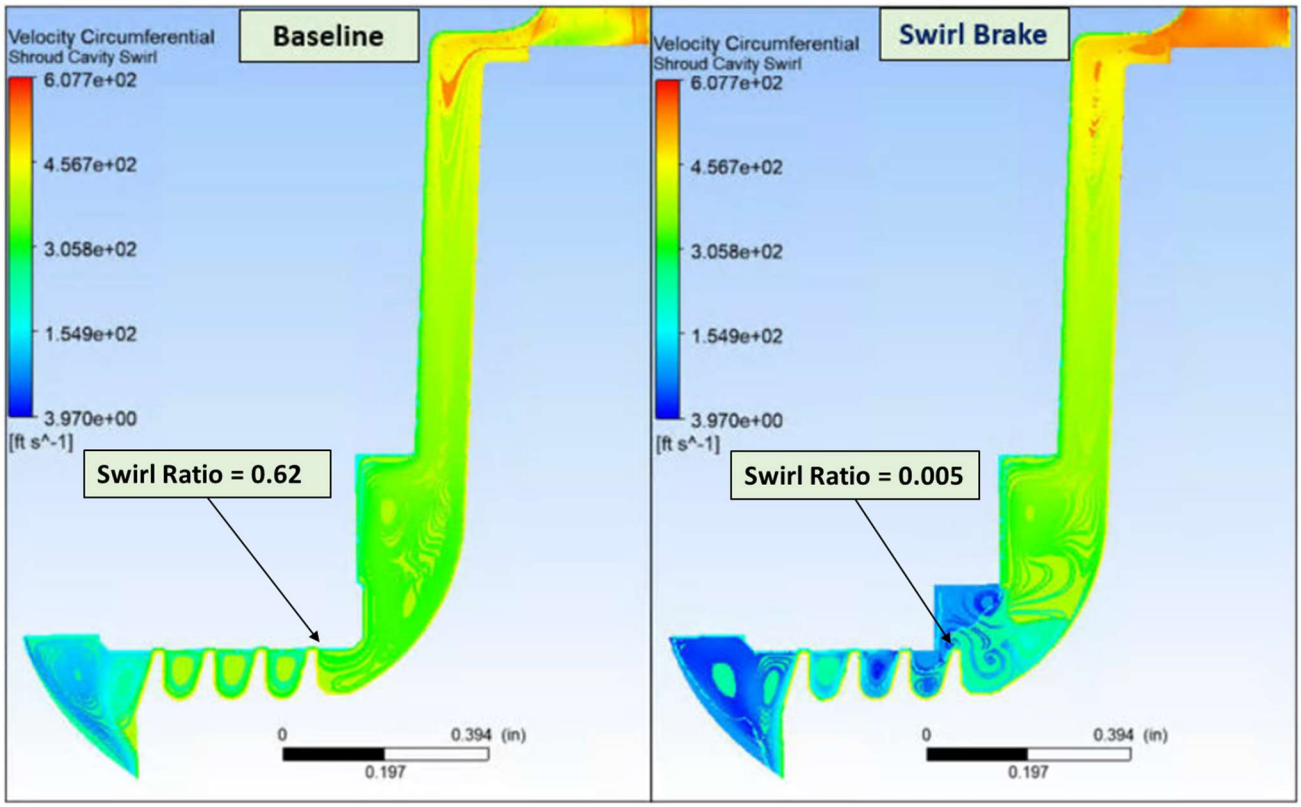

Figure 7. Comparison of fluid circumferential velocities between the Baseline and the SB models

Table 4. Comparison of circumferential velocities at teeth at the 2nd stage labyrinth eye seal

Location	Circumferential Velocity [m/s]	
	Baseline	with SBs
1st tooth	88.9	0.75
2nd tooth	89.4	11.6
3rd tooth	89.3	33.7
4th tooth	89.2	48.1

Figure 7 shows the calculated swirl velocity (circumferential flow) for the Baseline and the SB models. The swirl velocity comparison clearly shows that the SBs reduce the swirl velocity in the eye-seal. Table 4 shows the circumferential velocities at the four labyrinth seal tooth locations. The circumferential velocity was averaged over the plane of each tooth location. The circumferential velocity decreased significantly due to the SB obstruction, but slowly increased along the eye seal axially due to the tangential kinetic energy transferred to the fluid by the rotating shroud surface. The first tooth with swirl brakes saw a 99% reduction in swirl compared to the baseline case, while the subsequent three teeth experienced a reduction of 12% to 46% compared to the baseline case.

Table 5 lists area averaged swirl ratios at the 1st tooth of the eye seal. Swirl ratio is defined as the circumferential velocity divided by the impeller surface speed at seal inlet. The impeller surface speed at seal inlet is 142.9 m/s. The swirl ratios for the steady state CFD solution [15] and the time transient CFD solution are compared for the Baseline and the SB models. The time transient CFD predicts a higher swirl ratio (12%) than the steady state results for the Baseline case. A combination of the unsteady flow due to the physical offset

and the different treatment between the sliding interfaces in the time transient solution could have caused the differences in circumferential velocities. The time-transient CFD solution also predicts a near-zero swirl at the first tooth for the SB case. Overall, results from both methods (steady-state and transient CFD) show significant swirl reduction with the inclusion of the SB in the secondary leakage flow path.

Table 6 shows the comparison of seal leakage between the Baseline and the SB models. Since the SBs are located at the entrance of the eye seal, fluid flow characteristics through the 1st tooth are significantly different from the characteristics of the baseline case. The swirl brakes help generate free vortices just upstream of the first sealing tooth, the effect of which cascades through the remaining seal teeth. This causes an increase in the axial flow through the seal, thereby increasing the seal leakage. In the geometry analyzed, leakage increases by ~11% with SBs compared to the Baseline case. However, it must be noted that the increase in leakage is based on the secondary leakage flow, and not the stage flow itself. The predicted higher leakage is only about 0.02% of the overall flow rate of the impeller. With SBs on all 6 stages of the compressor, the overall compressor efficiency dropped less than 0.7%, as measured during the full-scale closed-loop test [15].

Table 5. Comparison of Swirl Ratios (2nd stage)

	Area Averaged Swirl Ratio at 1st tooth of eye seal	
	Steady State Solution [15]	Time Transient CFD solution
Baseline	0.55	0.62
SB	0.06	0.005

Table 6. Comparison of leakage flow (2nd stage)

	Leakage Flow (kg/s)
Baseline	0.17
SB	0.19

CFD ANALYSIS FOR CALCULATION OF ROTORDYNAMIC COEFFICIENTS

The fluid reaction forces in the impeller secondary flow passage can be modeled with the equations of motion (2) as described in previous research [5, 6, 11 and 17]. The reaction forces (F_x , F_y) produced by small amplitude motions (*X, Y*) of the rotor about its whirling center, as described in Equations (1) earlier, are given in [17] as:

$$-\begin{Bmatrix} F_x \\ F_y \end{Bmatrix} = \begin{bmatrix} K_{xx} & K_{xy} \\ -K_{yx} & K_{yy} \end{bmatrix} \begin{Bmatrix} X \\ Y \end{Bmatrix} + \begin{bmatrix} C_{xx} & C_{xy} \\ -C_{yx} & C_{yy} \end{bmatrix} \begin{Bmatrix} \dot{X} \\ \dot{Y} \end{Bmatrix} + \begin{bmatrix} M_{xx} & M_{xy} \\ -M_{yx} & M_{yy} \end{bmatrix} \begin{Bmatrix} \ddot{X} \\ \ddot{Y} \end{Bmatrix} \tag{2}$$

The [*K*], [*C*], [*M*] matrices denote the frequency independent stiffness, damping and inertia force coefficients. Substituting the rotor displacement from its whirling motion, Equation (1), into Equation (2), the force components become:

$$\begin{aligned} -\frac{F_x}{A} &= \left(K_{xx} + C_{xy}\Omega - M_{xx}\Omega^2\right)\cos(\Omega t) + \left(K_{xy} - C_{xx}\Omega - M_{xy}\Omega^2\right)\sin(\Omega t) \\ -\frac{F_y}{A} &= \left(-K_{yx} + C_{yy}\Omega + M_{yx}\Omega^2\right)\cos(\Omega t) + \left(K_{yy} + C_{yx}\Omega - M_{yy}\Omega^2\right)\sin(\Omega t) \end{aligned} \tag{3}$$

Notice that the reaction forces in the x and y-directions are normalized by the amplitude, A, of the whirling motion, resulting in the impedance in the two cartesian axes, x and y. For a circular whirling motion with an orbit of amplitude *A*, the rotordynamic coefficients are skew symmetric. The circular whirling motion yields the effective stiffness and damping as follows:

$$\begin{aligned} K_{eff} &= -\mathrm{Re}\left(\frac{F_x}{A}\right) = -Re\left(\frac{F_y}{A}\right) = K_{xx} + C_{xy}\Omega - M_{xx}\Omega^2 \\ \Omega C_{eff} &= \mathrm{Im}\left(\frac{F_x}{A}\right) = -Im\left(\frac{F_y}{A}\right) = -K_{xy} + C_{xx}\Omega + M_{xy}\Omega^2 \end{aligned} \tag{4}$$

The equations in (4) represent a linear, second-order model solution of (2). Each equation carries 3 unknowns, and hence they must

be solved implicitly using curve-fits. The equations must be run at multiple whirl frequencies to calculate the impedances at each of those whirl frequencies. The impedances thus obtained can then be curve-fit to calculate the six unknowns – i.e., the force coefficients.

Numerical time transient CFD solution is obtained for a given model (with or without SBs) at the given boundary conditions and a predetermined whirl frequency. The pressure profiles along the whirling shroud surface and along the rotating impeller surfaces are integrated to calculate the impedances. Care must be taken to handle the integration in the proper reference frames for the various surfaces – the impellers are solved with the rotating reference frame and the shroud surfaces in the cavity domain.

In this study, the transient simulations were performed for 5 different frequencies. The chosen frequencies were 0 Hz, 50 Hz, 100 Hz, 200 Hz and 312 Hz. For the 0 Hz case, the rotor spins without whirl at an off-centered position. Multiple orbit sizes, from 10-50% of the eye seal clearance in Equation (1), were evaluated for the test cases, but eventually, an orbit size A = 50% was chosen as a standard for all the analysis. K_{eff} and ΩC_{eff} were obtained by performing a fast Fourier Transform (FFT) on the reaction forces of the shroud surface from the time transient CFD analysis. Figure 8 and Figure 9 show the force impedances (dynamic stiffnesses) obtained from the Baseline and SB time transient CFD analyses. Curve-fits on the two curves result in frequency independent rotordynamic coefficients. The coefficient of determination, R^2, provides a measure of the goodness-of-fit while curve-fitting – it provides the fit correlation value for the linear regression model used on the impedances as a function of whirl frequencies. The fit correlation is roughly 95% for all cases. The deviations in the results were mostly caused from the reaction forces in the shroud cavity as the unsteady flow between the stator and the shroud surface is quite strong.

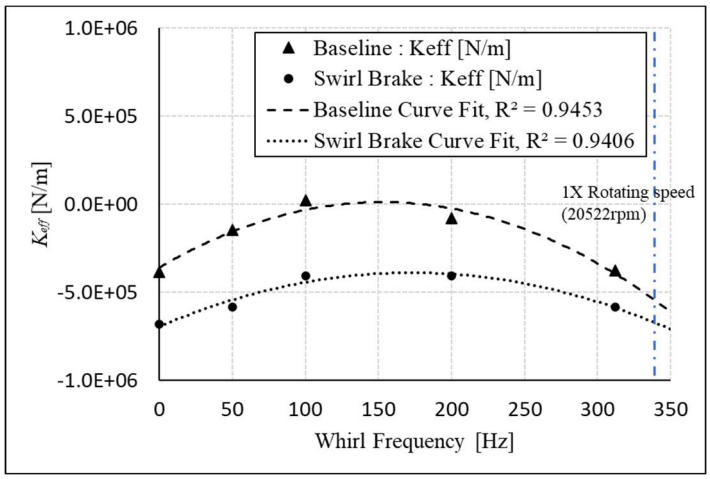

Figure 8. Effective stiffness K_{eff} vs. frequency. Comparison between Baseline and SB Models (2nd stage)

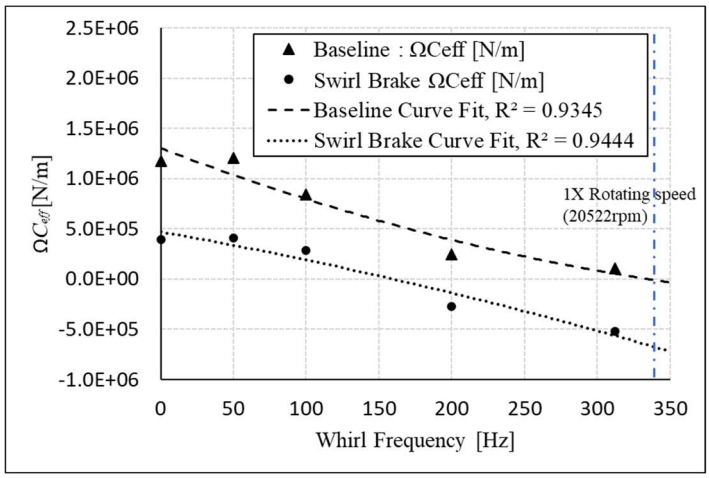

Figure 9. C_{eff} x Ω vs. frequency. Comparison between Baseline and SB Models (2nd stage)

Table 7 lists the rotordynamic coefficients estimated from the curve-fits of the linearized effective stiffness and effective damping impedance functions for the Baseline and the SB models. First, the impedance functions are generated for the seal + shroud domain and the force coefficients are obtained for this combined domain. In addition, there is an interest in understanding the effects of the eye seal separately from the shroud cavity itself. Since the shroud surface includes both the shroud cavity and the eye seal, the rotordynamic coefficients for the eye-seal and the shroud cavity could be obtained separately by post-processing the reaction forces from the individual

components. To estimate the impact of the eye seal and the shroud cavity separately, curve-fits are generated for the two regions separately, and the coefficients are generated again for each of the two regions (i.e., the eye-seal and the shroud cavity) separately. The total coefficients will be the sum of the force coefficients from the eye-seal and the shroud cavity.

Notice that, for the case without swirl brakes, the cross coupled stiffness from the shroud cavity is comparable to the cross coupled stiffness from the eye seal. The simulation appears to confirm the impact of shroud cavity on generating destabilizing forces. The cross-coupling forces in the shroud cavity arise from the strong fluid interaction between the rotor-stator surfaces, as the rotor continues to whirl. The shroud cavity is characterized by many recirculation zones amidst large changes in radius within a short axial distance, adding to the impact of swirl.

The cross coupled stiffness of the shroud cavity increased modestly with the addition of SB. It is indeed the steep drop of cross coupled stiffness in the eye seal that appears to result in a net drop of the combined eye seal-shroud cavity destabilizing forces. The direct damping of the eye seal is larger than the corresponding result for a shroud cavity, albeit the magnitude of damping is small. It is evident that the total cross coupled stiffness reduced significantly once the SB is in place. The eye seal cross coupled stiffness becomes negative due to the swirl reduction at the first tooth and lower along the seal. Overall, the SB reduces the cross coupled stiffness up to ~ 60% when compared to the results of the Baseline model.

From Equation (3), if the cross coupled mass, M_{xy}, is ignored, ΩC_{eff} becomes

$$\Omega C_{eff} = -K_{xy} + C_{xx}\Omega = -C_{xx}\omega\Omega_w\left(1 - \frac{f}{\Omega_w}\right) \tag{5}$$

where, $f = \Omega/\omega$ and ω = shaft rotational speed (*rad/s*). Ω_w is Whirl Frequency Ratio (WFR) which is defined as $\Omega_w = K_{xy}/C_{xx}\omega$. From the equation, an onset speed of instability is defined when f/Ω_w equals to one. If a rotor is whirling at its natural frequency, ω_n, the onset speed of instability becomes

$$\omega_s = \frac{\omega_n}{\Omega_w} \tag{6}$$

Figure 1 shows that the measured unstable natural frequency, ω_n, without SBs is 146Hz. The onset speed of instability, ω_s, is 296 Hz based on test data and field experience. Thus, WFR, Ω_w, without the SBs is calculated to 0.49 (=146 Hz/296 Hz) from the test result. The coefficients of the eye seal alone from the CFD analysis for the baseline case as shown in Table 7 show a WFR of 0.51, close to expectations. However, the predicted baseline WFR for the total system is 0.77. The overpredicted baseline WFR appears to be mainly caused by the shroud cavity. A closer look at the shroud cavity's coefficients shows that, while the cross-coupled stiffness is close to that of the eye seal, the direct damping from the shroud cavity is significantly low, resulting in an exceptionally high WFR. It is the authors' opinion that more work needs to be done on reassessing the wall shear-stress characteristics in the shroud region to better simulate the flow through the cavity and its effect on the tangential force impedance term.

Table 7. Rotordynamic Coefficients for secondary flow path from Baseline Model (2nd stage) and SB Model (2nd stage)

	Baseline	SB	Baseline	SB	Baseline	SB
	Total	Total	Eye Seal	Eye Seal	Shroud Cavity	Shroud Cavity
K_{xx} [N/m]	-422,931	-695,254	93,518	-208,576	-516,449	-486,677
K_{xy} [N/m]	1,261,439	470,566	713,817	-158,840	547,622	629,406
C_{xx} [N-s/m]	764	410	657	317	107	93
C_{xy} [N-s/m]	1,123	562	-123	27	1,245	536
M_{xx} [N-s^2/m]	0.0019	0.0008	0.0004	0.0001	0.0015	0.0006
M_{xy} [N-s^2/m]	0.0004	-0.0002	-0.0003	-0.00001	0.0006	-0.0002
$K_{xy} / C_{xx}\,\omega$	0.77	0.53	0.51	-0.23	2.39	3.15

The 5th stage of the compressor was also analyzed to evaluate the performance of the designed SB at higher operating pressure conditions. For this case, only the cross-coupled stiffness was calculated for both the Baseline and the SB models. Since the 5th stage has the same geometry as the 2nd stage, the same grid models were utilized for the CFD analysis. Table 8 lists the operating conditions for the 5th stage and Table 9 presents the cross coupled stiffness (K_{xy}) derived from the transient CFD analysis. The results also

demonstrate that the designed SB effectively reduces K_{xy} at high-pressure conditions. The reduction of K_{xy} is mainly caused by the eye seal providing a negative K_{xy} as in the 2nd stage results, due to substantial reduction in swirl velocities.

The eye seal of the 5th stage was analyzed with a labyrinth seal bulk flow model and the results were compared to those from CFD. The seal dimensions in Table 1 and the boundary conditions in Table 8 were utilized for the analysis. An inlet swirl ratio of 0.7 was applied at the eye seal. The bulk flow model predicted a cross coupled stiffness, K_{xy_bulk} , of 849,539 [N/m]. The CFD prediction for the eye seal is 12% larger than the bulk flow result.

Table 8. Boundary conditions (5th stage)

Rotating Speed	20,522 [rpm]
Inlet Pressure	10.89 [MPa]
Inlet temperature	141[°C]
Density at Inlet	86 [kg/m^3]
Outlet Pressure	12.54 [MPa]
Outlet Mass Flow Rate	9.48 [kg/s]
Fluid Density at Outlet	93 [kg/m^3]

Table 9. Comparison of cross coupled stiffness for 5th stage with transient CFD

	Baseline	With SB
	K_{xy} [N/m]	K_{xy} [N/m]
Total	1,769,657	321,883
Eye Seal	956,017	-360,761
Shroud Cavity	813,639	682,644

AERODYNAMIC CROSS COUPLING

Table 10 lists the cross coupled stiffness (K_{xy}) obtained from the current unsteady CFD model for the shroud cavity (Baseline model, w/o SB), as well as the coefficients produced by the Wachel formula [1], the API equation [2], and the Formula given by Moore and Ransom [6]. The boundary conditions in Table 3 and Table 8 were used to calculate the cross coupling for the respective stages in Table 9.

Table 10. Comparison of Aerodynamic Cross Coupling Coefficients for Shroud Cavity (only)

Method	Cross Coupling, K_{xy} [N/m]	
	2nd stage	5th stage
Transient CFD	547,622	813,639
Wachel [1]	439,919	424,332
API 617 [2]	471,091	454,454
Moore-Ransom [6]	411,373	478,447

The estimated K_{xy} from the three empirical models are close to each other for the 2nd and 5th stages. API 617 and Wachel's equations resulted in comparable K_{xy} due to the similar density ratios (discharge/inlet) for both the 2nd and 5th stages. The Moore-Ransom formula predicts a larger K_{xy} for the higher-pressure 5th stage. Relative to the empirical methods, the CFD-predicted K_{xy} is ~30% higher for the 2nd stage, and ~70% higher for the 5th stage.

The higher estimates from the CFD analysis (compared to the empirical models) arise primarily from modeling the pressure profile in the full shroud cavity. As mentioned earlier, the stage geometry and the 3D grid model for the 5th stage are identical to those of the 2nd stage. The higher K_{xy} for the 5th stage compared to the one for the 2nd stage is due to the difference in pressure drop and the increased density across compression stages.

Per API 617, the average gas densities at the operating conditions, shown in Table 1 and Table 5, are higher than the one specified

in the Level I criteria (3.75 lbf/ft^3) limit. Hence, a Level II analysis (using the rotordynamic coefficients for all stages) is required. Since only two stages were analyzed with the CFD analysis, the coefficients of other stages were estimated from simple interpolations of the coefficients for the 2nd and 5th stages. Moore et al. [6] showed that the direct damping coefficients rise at the same increment rate as the K_{xy}, hence yielding an almost constant WFR at the instability threshold. Using the assumption of constant WFR, the direct damping coefficients are estimated, as shown in Table 11.

Table 11. Estimated cross coupled stiffness and direct damping coefficients for all impellers at 20,522 rpm

	Cross Coupled stiffness, K_{xy} [N/m]						
	1st stage	2nd stage	3rd stage	4th stage	5th stage	6th stage	
Baseline	1,117,012	1,261,439	1,425,384	1,562,993	1,769,657	1,952,429	
SB	414,542	470,566	394,975	459,976	321,883	342,246	
	Direct Damping, C_{xx} [N-s/m]						WFR
	1st stage	2nd stage	3rd stage	4th stage	5th stage	6th stage	
Baseline	676	764	863	946	1,071	1,182	0.77
SB	361	410	344	401	280	298	0.53

STABILITY EVALUATION

This section presents the results of a lateral rotordynamic stability analysis for the 6-stage compressor with two tilting pad bearings located at both ends of the compressor. All analyses were performed with the same tilting pad bearings that were used for the full-scale testing [15]. Balance piston seal force coefficients were also incorporated within the lateral rotordynamics model to perform the stability analysis.

Table 12 shows the predicted log-dec and natural frequency for four different criteria: 1) no cross coupled stiffness coefficients added, 2) Level I analysis with cross coupling from API 617 standard, 3) Level II analysis with CFD results for the Baseline Model, and 4) Level II analysis with CFD results for the SB Model. Without any destabilizing forces added (K_{xy} =0), the predicted log-dec (δ) is positive, hence the simulation would indicate that the compressor would be stable. However, the measurements showed high sub-synchronous vibrations, see Figure 1. To predict the unstable operation, destabilizing cross coupling terms should be added to the "no cross coupling" case. The API Level I method that includes destabilizing forces predicts δ =0.15, which indicates that a Level II analysis may have to be conducted based on other criteria.

The Level II analysis of the rotor using the K_{xy} predicted by the CFD shows further reduction of the log dec. The predicted unstable frequency for baseline is 142 Hz showing 2.7% difference from the measured data in Figure 1 (a) of 146 Hz. Finally, a Level II analysis of the rotor model with SBs (using the cross-coupling coefficients predicted by CFD) yielded a log-dec, δ = 0.55. While no measured log dec exists to compare with the analytical results, the qualitative stability improvement can be distinctly observed in Figure 1 (b) with SBs.

Table 12. System log-dec (δ) and natural frequency from lateral rotordynamic stability analyses

	No cross-coupling forces Baseline	Level I API 617 [2] Baseline	Level II Time Transient CFD Baseline	Level II Time Transient CFD With SB
log-dec (δ)	0.57	0.15	0.03	0.55
Natural Frequency of the first mode	142 Hz	143 Hz	143 Hz	141 Hz

CONCLUSION

The present study shows a 3D transient CFD analysis of a centrifugal impeller with and without SBs in the TOR configuration to quantify the stability of a compressor with rotordynamic coefficients. The transient analysis with mesh deformation could successfully estimate the rotordynamic coefficients for an asymmetric geometry with SBs. The following conclusions are made based on the analysis results:

(a) With SBs, the swirl ratio at the inlet of the eye seal inlet significantly decreased.

(b) Without SBs, a larger cross coupled stiffness (K_{xy}) was predicted for the higher-pressure stage.

(c) The cross coupled stiffnesses of the shroud cavity with SBs reduced up to ~60% for the 2nd stage and ~80% for the 5th stage due to the negative cross coupled stiffness of the eye seal. The cross coupled stiffness of the shroud cavity rather slightly increased with SBs.

(d) Predictions of WFR with the transient CFD for the combined eye seal + shroud cavity is affected significantly by the shroud cavity results. More work is needed on this front to calibrate the impedance predictions on the shroud cavity to test data and field experience.

(e) The transient CFD analysis predicted higher aerodynamic cross coupling compared to existing empirical models (Wachel [1], API 617 [2], Moore et al. [6]) when using operating conditions where the compressor was unstable.

(f) For the cases analyzed, the transient CFD analysis predicted significantly higher aerodynamic cross coupling for the rear stage (high pressure stage) as compared to the front stage (low pressure stage), while the empirical models showed comparable level of cross coupling forces between 2nd and 5th stages.

(g) A level II analysis shows the stability improvement of the compressor with SBs by yielding a large, positive log dec, as qualitatively observed in the full-scale test results by Venkataraman et al. [15].

NOMENCLATURE

A	= Whirling Orbit	(L)
C	= Chord of the SB-slots	(L)
C, C_{xx}, C_{yy}	= Direct Damping Coefficients	(FT/L)
c, C_{xy}, C_{yx}	= Cross Coupled Damping Coefficients	(FT/L)
F_x, F_y	= Reaction Forces in X and Y directions	(F)
K, K_{xx}, K_{yy}	= Direct Stiffness Coefficients	(F/L)
k, K_{xy}, K_{yx}	= Cross Coupled Stiffness Coefficients	(F/L)
M, M_{xx}, M_{yy}	= Direct Mass Coefficients	(FT^2/L)
m, M_{xy}, M_{yx}	= Cross Coupled Mass Coefficients	(FT^2/L)
W	= Pitch of the SB-slots, fluid cavity only(L)	
X, Y	= Rotor Displacement	(L)
δ	= Logarithmic Decrement	
ω	= Shaft rotational Speed	(1/T)
ω_n	= Natural Frequency	(1/T)
Ω	= Whirl Frequency	(1/T)
Ω_s	= Onset Speed of Instability	(1/T)
Ω_w	= Whirl Frequency Ratio, WFR	

ABBREVIATIONS

OEM = Original equipment manufacturer
SB = Swirl Brake
TOR = Teeth on rotor
WFR = Whirl Frequency Ratio

REFERENCES

[1] Wachel, J. C., and von Nimitz, W. W., 1980, “Assuring the Reliability of Offshore Gas Compression Systems,” European Offshore Petroleum Conference & Exhibition, London, England, Oct. 21–24.

[2] API, 2014,“Axial and Centrifugal Compressors and Expander-Compressors,” API Standard 617 Eight Edition, American Petroleum Institute, Washington, DC

[3] Childs, D. W., 1989, “Fluid-Structure Interaction Forces at Pump-Impeller-Shroud Surfaces for Rotordynamic Calculations” Journal of Vibration, Acoustics, Stress, and Reliability in Design, Vol. 111, July, pp. 216-225.

[4] Bolleter, U., Wyss, A., Welte, I., and Sturchler, R., 1985, "Measurement of Hydrodynamic Matrices of Boiler Feed Pump Impellers," ASME Paper 85- DET-147, 10th Biennial Conference on Mechanical Vibration and Noise, Cincinnati, Ohio, September

10-13.

[5] Moore, J.J., and Palazzolo, A.B., 1999, “Rotordynamic Force Prediction of Whirling Centrifugal Impeller Shroud Passages Using Computational Fluid Dynamic Techniques,” ASME Paper No 99-GT- 334.

[6] Moore, J. J., Ransom, D. L., and Viana, F., 2011 "Rotordynamic Force Prediction of Centrifugal Compressor Impellers Using Computational Fluid Dynamics." Journal of Engineering for Gas Turbines and Power, Vol. 133, 042504.

[7] Chochua, G., and Soulas, T. A., 2007. "Numerical modeling of rotordynamic coefficients for deliberately roughened stator gas annular seals." Journal of tribology, Vol 129.2: 424-429

[8] Xin, Y., Li, j., Feng, Z., 2011. "Investigations on the Rotordynamic Characteristics of a Hole-Pattern Seal Using Transient CFD and Periodic Circular Orbit Model." Journal of vibration and Acoustics, Vol. 133, 041007.

[9] Li, Zhigang, Jun Li, and Xin Yan. "Multiple Frequencies Elliptical Whirling Orbit Model and Transient RANS Solution Approach to Rotordynamic Coefficients of Annual Gas Seals Prediction." Journal of Vibration and Acoustics 135.3 (2013): 031005.

[10] Yan, X., He, K., Li, j., Feng, Z., 2015. "A generalized prediction method for rotordynamic coefficients of annular gas seals." Journal of Engineering for Gas Turbines and Power 137.9 (2015): 092506.

[11] Hoopes, K., Moore, J. J., Rimpel, A., Kulhanek, C., Venkataraman, B., 2019, “A Method for Rotordynamic Force Prediction of a Centrifugal Compressor Impeller Front Cavity Using a Transient Whirling CFD Technique,” Proceedings of ASME Turbo Expo, Phoenix, Arizona, June 17-21, GT2019-91904

[12] Nielsen, K.K., Myllerup, C.M., and Van den Braembussche, R. A., 1998, “Optimization of Swirl Brakes by Means of a 3D Navier-Stokes Solver, ASME Paper 98-GT-328.

[13] Moore, J. and Hill, D., 2000, “Design of Swirl Brakes for High Pressure Centrifugal Compressors Using CFD Techniques”, International Symposium on Transport Phenomena and Dynamics of Rotating Machinery, Honolulu, Hawaii.

[14] Baldassarre, L., Bernocchi, A., Fontana, M., Guglielmo, A., and Masi, G., 2014, “Optimization of Swirl Brake Design and Assessment of its Stabilizing Effect on Compressor Rotordynamic Performance”, Proceedings of the 43rd Turbomachinery Symposium, Turbomachinery Laboratory, Texas A&M University, College Station, Texas.

[15] Venkataraman, B., Moulton, D., Cave, M., Clarke, C., Wilkes, J., Moore, J. J., and Eldridge, T., 2018, “Design and Implementation of Swirl Brakes for Enhanced Rotordynamic Stability in an Off-shore Centrifugal Compressor,” Proceedings of Asia Turbomachinery and Pump Symposium, May 12-15, Singapore. 172529.

[16] Menter, F. R., Kuntz, M., & Langtry, R. 2003, “Ten years of industrial experience with the SST turbulence model.” In K. Hanjalic, Y. Nagano, & M. Tummers (Eds.), Turbulence, heat and mass transfer 4 (pp. 625–632). New York, NY: Begell House.

[17] Childs, D. W., 1993, Turbomachinery Rotordynamics, John Wiley & Sons, New York, New York

ACKNOWLEDGEMENT

The authors wish to thank Solar Turbines Inc. for allowing to publish the work, and David Moulton and Mike Cave for the support with the design of the swirl brakes.